Critical behaviour of the Ising ferromagnet confined in quasi-cylindrical pores: A Monte Carlo study

Leandro E. Guisandez, Guillermo J. Zarragoicoechea, and Ezequiel V. Albano

Citation: The Journal of Chemical Physics **139**, 154706 (2013); doi: 10.1063/1.4821826
View online: http://dx.doi.org/10.1063/1.4821826
View Table of Contents: http://scitation.aip.org/content/aip/journal/jcp/139/15?ver=pdfcov
Published by the AIP Publishing

Critical behaviour of the Ising ferromagnet confined in quasi-cylindrical pores: A Monte Carlo study

Leandro E. Guisandez,[1] Guillermo J. Zarragoicoechea,[1,2] and Ezequiel V. Albano[1,3]
[1]*Instituto de Física de Líquidos y Sistemas Biológicos (IFLYSIB), Universidad Nacional de La Plata, CONICET CCT-La Plata, Calle 59 Nro 789, (1900) La Plata, Argentina*
[2]*Comisión de Investigaciones Científicas de la Provincia de Buenos Aires, Argentina*
[3]*Departamento de Física, Facultad de Ciencias Exactas, Universidad Nacional de La Plata, La Plata, Argentina*

(Received 29 March 2013; accepted 6 September 2013; published online 16 October 2013)

The critical behaviour of the Ising ferromagnet confined in pores of radius R and length L is studied by means of Monte Carlo computer simulations. Quasi-cylindrical pores are obtained by replicating n-times a triangular lattice disc of radius R, where $L = na$ and a is the spacing between consecutive replications. So, spins placed at the surface of the pores have less nearest-neighbours (NN) as compared to 8 NN for spins in the bulk. These "missing neighbour" effects undergone by surface spins cause a strong suppression of surface ordering, leading to an ordinary surface transition. Also, the effect propagates into the bulk for small tubes ($R \leq 12$) and the effective critical temperature of the pores is shifted towards lower values than in the bulk case. By applying the standard finite-size scaling theory, subsequently supported by numerical data, we concluded that data collapse of relevant observables, e.g., magnetization (m), susceptibility, specific heat, etc., can only be observed by comparing simulation results obtained by keeping the aspect ratio $C \equiv R/L$ constant. Also, by extrapolating "effective" R-dependent critical temperatures to the thermodynamic limit ($R \to \infty$, C fixed), we obtained $T_C(\infty) = 6.208(4)$. As suggested by finite-size scaling arguments, the magnetization is measured at the critical point scales according to $\langle |m| \rangle_{T_c} R^{\frac{\beta}{\nu}} \propto \left[\frac{R}{L}\right]^{\frac{1}{2}}$, where β and ν are the standard exponents for the order parameter and the correlation length, respectively. Furthermore, it is shown that close to criticality the axial correlation length decreases exponentially with the distance. That result is the signature of the formation of (randomly distributed) alternating domains of different magnetization, which can be directly observed by means of snapshot configurations, whose typical length (ξ) is given by the characteristic length of the exponential decay of correlations. Moreover, we show that at criticality $\xi = 0.43(2)R$. © *2013 AIP Publishing LLC*. [http://dx.doi.org/10.1063/1.4821826]

I. INTRODUCTION

The study and understanding of phase transitions and critical phenomena that take place in confined geometries are topics of both fundamental and practical interest, which have recently attracted considerable attention.[1–4] The interplay between the finite-size of the confinement geometry and the surface effects due to the interaction of the physical system with the walls of the container modifies the phase behaviour of the confined system as compared to the bulk.[5–9] In fact, phase transitions are often shifted due to surface effects and rounded due to finite-size effects.[10–12] Furthermore, and due to the purpose of this paper that focuses on the critical behaviour of fluids and fluid mixtures in nano- and micro-pores, one also has a topic with many technological and practical applications[13,14] ranging from the non-conventional extraction of gas and oil from porous clays and rocks to the design and operation of nano- and micro-fluidic devices.[4,15] In addition, the study of gas adsorption in tubes at the nanoscale has been boosted by the development and availability of several techniques to synthesise carbon nanotubes, e.g., the laser vaporization synthesis method, which is of particular interest since it allows one to obtain ordered carbon nanotube structures. Namely, the mentioned method produces "ropes" that typically have 10–20 nm of diameter and lengths over 100 μm, as observed by Scanning Electron Microscope (SEM) imaging.[16] On the other hand, Transmission Electron Microscopy (TEM) observations[16] show that these ropes are actually arrays of several single-wall carbon nanotubes that axially look like a bi-dimensional honeycomb of lattice constant 1.7 nm and where each cell of the honeycomb is a carbon nanotube separated from the others by at least 0.315 nm. Furthermore, the single-wall carbon nanotubes have a diameter of 1.38±0.02 nm and are bonded by weak inter-tube van der Waals forces.

Motivated by these technical and experimental applications, we will treat the topic, however, from a more fundamental point of view, i.e., by addressing its statistical mechanics description by means of an archetypical model: the confined Ising ferromagnet. Along the paper we will use the magnetic terminology, without losing generality, since the mapping of the Ising model into a lattice gas allows for a straightforward description in terms of a confined fluid. The same prescription also holds for the properties of a confined binary alloy.[17]

It is worth mentioning that the 3D Ising ferromagnet confined by parallel walls that exert competing short-range surface magnetic fields has been extensively studied[12,18–20] in order to characterize wetting phenomena, i.e., the

localization-delocalization transition of the interface between magnetic domains of different orientation, which is the precursor of the wetting phase transition that takes place in the thermodynamic limit only.[21] Similar studies have also been performed in 2D, where some existing exact results have been confirmed by means of Monte Carlo simulations.[22] Also, by adopting the wedge geometry, with competing magnetic fields, the so-called filling transition has also been studied by means of Monte Carlo simulations of the Ising magnet.[23–25] For studies of their 2D counterpart, i.e., the corner filling transition, see Ref. 26. Very recently, the Ising magnet was also employed for the study of both capillary condensation and the rounding of phase transitions in cylindrical pores.[10,27] The former case was also studied in 2D by adopting a rectangular ($L \times D$, $L \gg D$) geometry, i.e., by actually using long strips (for early studies of this system performed by keeping the aspect ratio $D/L = constant$ see also Ref. 28). Furthermore, in long pores, by scanning the bulk magnetic field H, hysteresis effects of the magnetization are identified; in particular, the fact that the area enclosed by hysteresis curves strongly decreases while increasing T, and for $T > T_0(L, D)$, i.e., temperatures higher than the hysteresis critical point, hysteresis is no longer observed. For $H = 0$ and $T < T_0(L, D)$ the probability distribution of the order parameter, $P(M)$, exhibits two peaks at the exactly known spontaneous magnetization of the system. However, for $T > T_0(L, D)$ a broad peak at $M = 0$ appears and is identified with the onset of a multi-domain configuration, as was also observed earlier.[27] In addition, capillary condensation was actually studied in cylindrical pores with and without surface magnetic fields.[10] The study is mainly focused on the case of large pores, i.e., $L \gg R$, where L and R are the length and the radius of the pores, respectively. It is found that the nature of the phase coexistence at the vapour-liquid transition (note that here we are adopting the lattice-gas terminology) strongly depends on the length of the pore or cylinder: for very long pores the system is axially homogeneous at low T, while at high temperatures, but still far below criticality, the system becomes axially inhomogeneous exhibiting a multi-domain structure such that liquid-liquid and vapour-liquid domains alternate along the tube.

Within the broad context discussed above, it is worth mentioning that here we adopt an alternative approach for the study of critical phenomena in quasi-cylindrical pores, namely, we will focus our interest on samples where the aspect ratio $C \equiv R/L$ is kept constant, so that our results can straightforwardly be extrapolated to the thermodynamic limit in order to characterise a true phase transition. So, our aim is to characterise the critical behaviour of the Ising ferromagnet confined in quasi-cylindrical pores by means of finite-size scaling analysis of equilibrium Monte Carlo measurements. It is worth mentioning that finite-size scaling quantities depend not only on the universality class of the phase transition, but also on the geometry and boundary conditions used. Of course, the model proposed for the adsorption in the pores is rather specific; however, in the regime where the correlation length ξ becomes much larger than the lattice spacing, one expects to enter into a universal scaling regime such that the microscopic details of the model become irrelevant.[29]

It is also worth mentioning that our study is performed by assuming the absence of both surface and bulk magnetic fields and, therefore, it represents a quite different approach from the one used in Refs. 10 and 27, that on the other hand is focused to the study of hysteresis effects and capillary condensation.

Finally, we would like to mention that the critical Casimir effect, which is observed in confined geometries,[30] has recently attracted much interest.[31,32] Also, it is interesting to note that incidentally the Casimir force is found in some cases to be dependent on the aspect ratio of the confining geometry.[31,32] Nevertheless, this work is not intended to deal with that effect but it will be considered in future studies.

The paper is organized as follows: in Sec. II we provide a description of the Ising magnet confined in quasi-cylindrical pores. Section III is dedicated to the presentation and discussion of the relevant theoretical background. The details of the Monte Carlo simulation method used and our results are then presented and discussed in Sec. IV, while our conclusions are finally stated in Sec. V.

II. ISING MAGNET CONFINED IN QUASI-CYLINDRICAL PORES

In order to represent the quasi-cylindrical tubes or pores in a simplified way, we consider a triangular 2D lattice disc of arbitrary radius R (see Figure 1) and replicate it $n = L/a$ times in order to obtain the desired 3D lattice. Typically, we choose $a = 1$ for the spacing between successive replications and an aspect ratio of $C \equiv R/L = 1/12$. By adopting this configuration, except for the sites on the surface, each site of the 3D lattice has eight neighbours, namely, six corresponding to the plane where the site belongs to and two corresponding to the neighbouring disc replications. Furthermore, in order

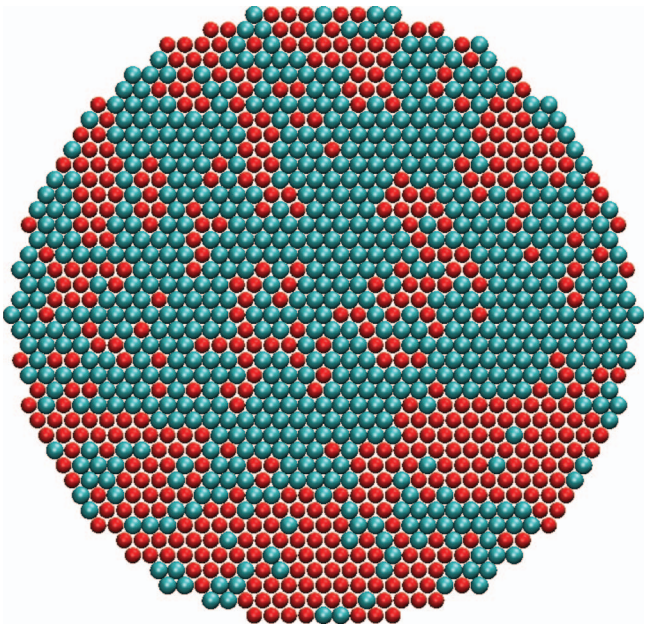

FIG. 1. Typical snapshot of the triangular lattice disc of radius $R = 18$ where colors differentiate up and down spins. Note that in this top view of the quasi cylindrical pore, each spin is surrounded by six nearest neighbors.

to implement the confined geometry, we choose periodic boundary conditions at the extremes of the tube in order to avoid unpleasant boundary effects, while free boundary conditions are assumed for the quasi-circular surface of the tube. Also, for the sake of simplicity, we choose the distance and the strength of the interaction among the sites within and out of the plane to be the same but, of course, this hypothesis could be relaxed in order to depict a more general situation. We also assume that each site of the above-defined lattice is occupied by a spin that can adopt only two orientations, namely, $s = \pm 1$. Then, the confined ferromagnet is represented by a typical 3D-Ising Hamiltonian, $\mathcal{H}$, namely,

$$\mathcal{H} = -J \sum_{\{nm\}} s_n s_m, \tag{1}$$

where the sum is taken over the eight next-near neighbours previously mentioned and is denoted by $\{nm\}$. In this case we consider that neither bulk nor surface fields are present on the system.

In order to achieve the characterization of the system we performed Monte Carlo simulations. For the simulations we adopt the single spin flip with the Metropolis algorithm. So, a randomly selected spin is flipped with probability $p_{flip} = \exp(-\frac{\Delta\mathcal{H}}{k_B T})$, where $\Delta\mathcal{H}$ is the energy change involved in the process, T is the temperature, and k_B is the Boltzmann constant. Henceforth, T is reported in units of J/k_B. A Monte Carlo time step (MCs) involves $N_R L$ flipping attempts, where N_R is the number of sites belonging to a disc of radius R. In this way, during a single MCs each site of the sample is selected once on average.

In order to perform equilibrium measurements, we start the simulations from a random distribution of spins, and the first N_D MCs are discarded to allow for equilibration. Typical simulations involve $N_T = 1 \times 10^6$ MCs. Then, after disregarding $N_D = 0.5 \times 10^6$ MCs, the relevant observables (see below) are measured and stored. Measurements are performed at different temperatures within the range $5.2 \leq T \leq 6.8$ and by using cylinders of different sizes, i.e., typically we used radii $R = 6$, 9, 12, 18, 24, and 36. In most simulations we kept the aspect ratio $C = \frac{R}{L} = 1/12$ constant. Along this paper we restrict ourselves to the case of null magnetic fields acting on both the bulk ($H_b = 0$) and the surface ($H_s = 0$), see Eq. (1). Subsequently, thermal averages (denoted by $\langle \dots \rangle$) of relevant observables are measured during $N_M = (N_T - N_D)$ MCs. We typically measure the order parameter, i.e., the magnetization per spin, given by

$$\langle m \rangle = \left\langle \frac{1}{N_s} \sum_{i,j,k} s(i, j, k) \right\rangle, \tag{2}$$

where $N_s \propto R^2 L$ is the total number of spins in the sample and the summation is taken over all spins in the 3D lattice identified by coordinates (i, j, k). As usually happens in finite systems, along the simulation, the magnetization may perform excursions between values close to $\pm M_s$, where M_s is the spontaneous magnetization, so that the thermal average, as defined by Eq. (2), simply vanishes. In order to overcome this shortcoming, one actually measures the average of the absolute magnetization $\langle |m| \rangle$.

The other relevant observables measured along the simulations are the susceptibility given by the fluctuation of the order parameter, namely,

$$\chi = \frac{N_s}{k_B T} (\langle M^2 \rangle - \langle M \rangle^2), \tag{3}$$

where M is the total magnetisation and the energy per spin measured in units of J,

$$E = \left\langle \frac{1}{N_s} \sum_{i,j,k} \sum_{\{i,j,k\}} s(i, j, k) s(\{i, j, k\}) \right\rangle, \tag{4}$$

where the curly brackets indicate that the sum is over all the eight neighbours of the (i, j, k) spin. The specific heat,

$$C_V = \frac{N_s}{k_B T^2} (\langle E^2 \rangle - \langle E \rangle^2), \tag{5}$$

is measured too.

It is also interesting to study the magnetization profiles that show the value of the average magnetization for an inner radius, r, of the pore given by

$$\langle m(r) \rangle = \left\langle \frac{1}{N_r} \sum_{i(r), j(r), k} s(i(r), j(r), k) \right\rangle, \tag{6}$$

where the sum is over all values of k and those values of $i(r)$ and $j(r)$ that satisfy $r^2 = i(r)^2 + j(r)^2$, and N_r is the number of spins at the inner radius, r.

As was already mentioned in Sec. I, it is expected that close but below criticality the system would exhibit an inhomogeneous pattern that consists of alternating domains of opposite spin orientation.[27] In order to estimate the size of the domains, it is useful to measure the axial spin-spin correlation

$$g(l) = \frac{1}{N_l} \sum_{k=1}^{L/2} \sigma(k) \sigma(k + l), \tag{7}$$

where $\sigma(k)$ is the average value of the spins at the kth layers and N_l is the normalization factor. In fact, since the above-mentioned domains occur axially,[27] it is natural to calculate the correlation along the tube and not radially.

III. THEORETICAL BACKGROUND: FINITE-SIZE SCALING APPROACH APPLIED TO EQUILIBRIUM MEASUREMENTS

It is widely accepted that, close to criticality, thermodynamic potentials can be expressed as the sum of a regular and a singular part, where the latter is a homogeneous function and describes the phase transition.[5,33] Recall that an n-argument function f is homogeneous of degree $\{\sigma\}$ if it satisfies

$$\lambda f(x_1, x_2, \dots, x_n) = \tilde{f}(x_1 \lambda^{\sigma_1}, x_2 \lambda^{\sigma_2}, \dots, x_n \lambda^{\sigma_n}),$$

where $\lambda \in (0, \infty)$ and σ_i defines the homogeneous degree of x_i, $i = 1, \dots, n$. In particular, by choosing $\lambda = |x_1|^{-1/\sigma_1}$ one obtains

$$|x_1|^{-1/\sigma_1} f(x_1, x_2, \dots, x_n) = \tilde{f}(\pm 1, |x_1|^{-\sigma_2/\sigma_1} x_2, \dots, |x_1|^{-\sigma_n/\sigma_1} x_n),$$

which shows up as an interesting feature of systems at criticality: since the scaling function $\tilde{f}$ does not depend on x_1, data sets corresponding to different x_1 collapse onto the same subspace given by $\tilde{f}$, or equivalently, by $|x_1|^{-1/\sigma_1} f(x_1, \ldots, x_n)$. Usually, the function f is the free energy, from which any relevant observable might be obtained, and the scaling variables are control parameters such as the temperature or magnetic field, as in the Ising model. Nonetheless, when dealing with finite-size systems, as in our case, the ratio between the linear dimensions of the system, R and L, and the microscopic distance, a (e.g., the lattice spacing that might be taken as $a = 1$), i.e., $N_R = R/a = R$ and $N_L = L/a = L$ become relevant scaling variables too. Furthermore, since there are no magnetic fields and the spin-spin interaction depends only on the distance, the pore possesses isotropic critical behaviour, so the scaling relationship for the magnetization is given by[34]

$$\langle |m| \rangle = R^{-\beta/\nu} \tilde{M}(R/\xi_b, R/L) = R^{-\beta/\nu} \tilde{\tilde{M}}(\epsilon R^{1/\nu}, R/L), \tag{8}$$

where $\epsilon = 1 - \frac{T}{T_c}$, T_c is the critical temperature. Here, we used the fact that the infinite-volume correlation length ξ_b diverges as $\xi_b \propto |\epsilon|^{-\nu}$, ν being the correlation length exponent. Furthermore, in the thermodynamic limit the magnetization vanishes as $\langle |M| \rangle \propto |\epsilon|^{\beta}$, where β is the critical exponent of the order parameter.[35] Then, the fluctuations of the magnetization yield the susceptibility (χ), as follows:

$$k_B T \chi = R^{\gamma/\nu} \tilde{\chi}(R/\xi_b, R/L) = R^{\gamma/\nu} \tilde{\tilde{\chi}}(\epsilon R^{1/\nu}, R/L). \tag{9}$$

It is worth mentioning that the above scaling arguments hold only if, taking $R \to \infty$ and $\epsilon \to 0$, both $\epsilon R^{1/\nu}$ and the aspect ratio R/L are kept constant. As is well known, these finite-size scaling results are usually used to test the validity of the critical temperature and exponent values. On the other hand, the system that we are dealing with possesses a clear anisotropic geometry, i.e., the typical longitudinal size in one of the three dimensions (L) differs from the two remaining (equivalent) radial sizes (R). This anisotropy, in turn, suggests that critical correlations would be limited by the shortest dimension or, in other words, we expect that the finite-volume correlation length behaves as $\xi \propto R$.

At criticality the magnetization features a particular dependence with the aspect ratio. This can be seen taking $\epsilon = 0$ in Eq. (9) so the scaled susceptibility depends only on the aspect ratio,

$$k_B T \chi = R^{\gamma/\nu} \tilde{\tilde{\chi}}(R/L) = R^{d-2\beta/\nu} \tilde{\tilde{\chi}}(R/L), \tag{10}$$

where the hyperscaling relation

$$\gamma/\nu = 2 - \eta = d - 2\beta/\nu \tag{11}$$

was used in the last equality and $d = 3$ is the dimensionality of the system. On the other hand, at $T = T_c$, the magnetization is proportional to $\sqrt{\langle m^2 \rangle}$ and can be related to the susceptibility[28]

$$\langle |m| \rangle_{T_c} \propto \sqrt{\frac{k_B T_c \chi(T_c)}{N_s}}. \tag{12}$$

Then, using the last term of Eq. (10) and the already mentioned fact that $N_s \propto LR^2$, we obtain

$$\langle |m| \rangle_{T_c} \propto \left[\frac{R^{3-2\beta/\nu}}{LR^2} \tilde{\tilde{\chi}}(R/L) \right]^{1/2} = R^{-\beta/\nu} [R/L]^{1/2} [\tilde{\tilde{\chi}}(R/L)]^{1/2}, \tag{13}$$

or more explicitly,

$$\langle |m| \rangle_{T_c} R^{-\beta/\nu} \propto \left[\frac{R}{L} \right]^{1/2}, \tag{14}$$

which means that at criticality the scaled magnetization per spin depends on the square root of the aspect ratio.

As already mentioned above, finite-size effects shift the peaks of the specific heat and the susceptibility with respect to the thermodynamic limit. This means that, in finite systems, one can only measure effective critical temperatures that depend on the radius of the pore, $T_c(R)$, and can be identified by the location of the maxima of the above mentioned observables. In particular, enlarging the radius of the tube, one asymptotically arrives at the thermodynamic limit, i.e., at the critical temperature of the bulk. In order to estimate the critical temperature, we use the fact that the effective critical temperatures of the tubes as a function of the radius can be expressed as[36,37]

$$T_c(R) = A + \alpha \left[\frac{1}{R} \right]^{1/\nu}, \tag{15}$$

where

$$A = \lim_{R \to \infty} T_c(R), \tag{16}$$

α is a constant, and the aspect ratio $C \equiv R/L$ of the sample is kept constant.

On the other hand, close to T_c the correlation function becomes isotropic and can be expressed in terms of a scaling function $g^*(r = (x^2 + y^2 + z^2)^{1/2})$, given by[28]

$$g(r) = r^{-\eta} g^* \left(\frac{r}{\xi_b} \right) \quad \text{with} \quad \xi_b \propto |\epsilon|^{-\nu}, \tag{17}$$

where the critical exponents are related via scaling relationships, e.g., Eq. (11). However, in the case of long tubes it is convenient to consider the limit $L \to \infty$, but keeping the radius R fixed. So, the system becomes quasi-one-dimensional and stays disordered for all finite temperatures. Then, it is expected that the correlation function, as defined by Eq. (7), would decay exponentially,[38,39] i.e.,

$$g(l) \propto \exp^{-\frac{l}{\xi}}, \tag{18}$$

with

$$\xi = BR, \tag{19}$$

where B is a constant and ξ can be identified as the characteristic correlation length that provides the averaged length of the alternating domains. So, Eq. (17) can be rewritten as

$$g(l) \propto R^{-\eta} g^* \left(\frac{l}{BR} \right). \tag{20}$$

It is worth mentioning that the pre-factor B in Eq. (19) depends on the type of boundary conditions used and it is not

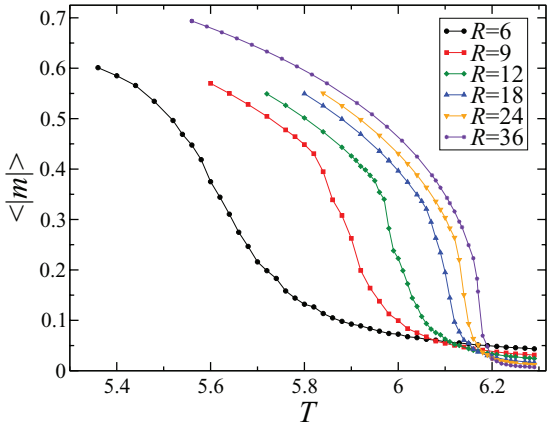

FIG. 2. Plots of the absolute magnetization per spin, $\langle|m|\rangle$ versus T, as obtained for cylinders of different sizes. The aspect ratio $C = R/L = 1/12$ is kept constant. For more details see text.

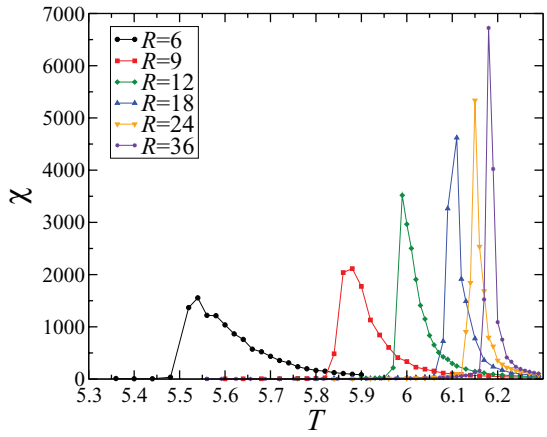

FIG. 3. Plots of the susceptibility, χ, versus T as obtained for cylinders of different sizes. The aspect ratio $C = R/L = 1/12$ is kept constant. For more details see text.

set by scaling arguments. Also, it can be evaluated by conformal invariance in 2D.[40]

IV. SIMULATION RESULTS AND DISCUSSION

Figure 2 shows the temperature dependence of magnetization per spin $\langle|M|\rangle$ corresponding to cylinders of different radii. Here one observes a dramatic shift of the curves towards lower temperatures for cylinders of small radii. This is a typical shifting effect of the "effective" critical temperature caused by the finite size of the samples. Also, rounding of the curves can be observed, mainly due to the action of surface effects of the cylinders. It is worth mentioning that the most significant drop in magnetization, which corresponds to the cylinder with $R = 36$, takes place close to T ~6.2, i.e., a temperature far above the critical temperatures of both the 3D Ising model in the square lattice given by $T_{SL_{3D}} = 4.51142(5)$[37] and the 2D Ising triangular lattice given by $T_{triang_{2D}} = 3.6410$.[41] Of course, the actual critical temperature of the replication of the 2D triangular lattice, which we performed along its perpendicular axis in order to mimic the cylinders, is expected to be different from the above-mentioned figures (e.g., larger than $T_{SL_{3D}}$ due to the fact that now one has two additional NN spins), as confirmed below by means of a finite-size extrapolation to the thermodynamic limit. On the other hand, our estimation is close to $T_{hypercub_{4D}} = 6.682(2)$,[42] the critical temperature of the 4D Ising hyper-cubic lattice, where, as in our case, each spin has eight neighbours.

Figures 3 and 4 show plots of the susceptibility, χ, and the specific heat, C_V, versus T as obtained for cylinders of different radii, respectively. Here, one observes well defined peaks of both χ and C_V that also occur at different well-defined temperatures, $T^{\chi}(R)$ and $T^{C_V}(R)$, respectively. As is implied in the adopted notation, these temperatures depend on the sample size and can be identified as "effective" pseudo-critical temperatures of finite systems. In fact, by proper extrapolation to the thermodynamic limit according to Eq. (15), it is possible to determine the critical temperature of the Ising magnet in our lattice (cf. Figure 5). The extrapolations of

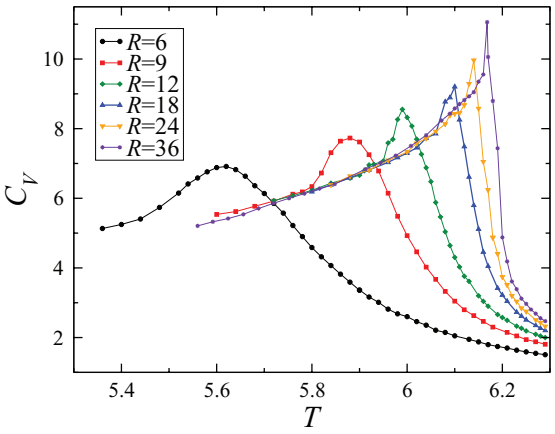

FIG. 4. Plots of the specific heat, C_v, versus T as obtained for cylinders of different sizes. The aspect ratio $C = R/L = 1/12$ is kept constant. More details are given in the text.

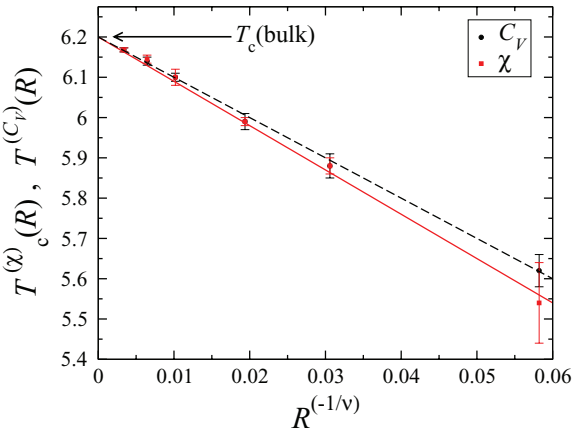

FIG. 5. Plots of $T^{\chi}(R)$ and $T^{C_V}(R)$ (full squares and circles, respectively) versus $R^{-1/\nu}$ as obtained by taking $\nu = 0.63002(10)$[43] corresponding to the 3D-Ising model. The straight lines correspond to the best fits of the data according to Eq. (15). The arrow shows the critical temperature extrapolated to the thermodynamic limit given by $T_c^{\chi} = 6.2(3)$ and $T_c^{C_V} = 6.2(1)$ for the susceptibility and the specific heat, respectively. More details are given in the text.

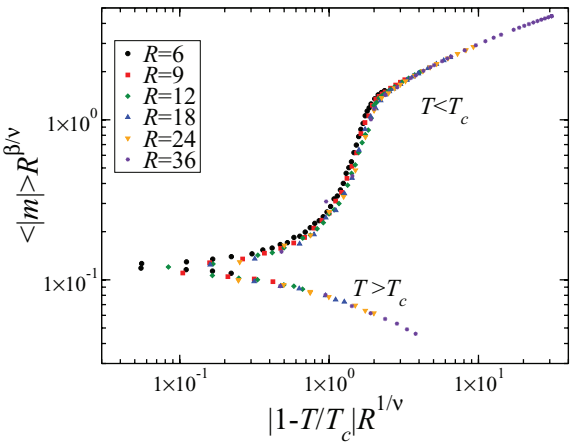

FIG. 6. Log-log plot for the scaling of the absolute magnetization per spin obtained according to Eq. (8) by using the data already shown in Figure 1 and taking $T_c = 6.208$, $\nu = 0.63002$, and $\beta = 0.3265$.

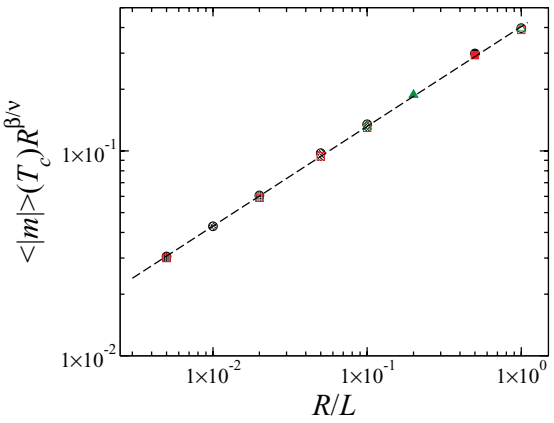

FIG. 8. Log-log plot of the scaled absolute magnetization per spin at $T_c = 6.208$, $\langle |M| \rangle (T_c) R^{-\beta/\nu}$, versus the aspect ratio $C = R/L$. Circles, squares, and triangles correspond to $R = 6$, 9, and 12, respectively. The dashed line corresponds to the best fit of the data that yields a slope of 0.486(6). The aspect ratios used were $L/R = 1$, 1/2, 1/10, 1/20, 1/50, 1/100, and 1/200. The critical exponents used were those of the Ising 3D model, namely, $\nu = 0.63002$ and $\beta = 0.3265$. More details are given in the text.

the data corresponding to χ and C_V yield $T_c^{(\chi)} = 6.2(3)$ and $T_c^{(C_V)} = 6.2(1)$, respectively.

After an approximate determination of T_c we are in a condition to attempt the achievement of data collapse of relevant observables in order to test the validity of the scaling relations (8) and (9) as shown in Figures 6 and 7, respectively. At this point it is worth mentioning that we assume that the system belongs to the 3D-Ising universality class, hence we will make use of reported values[43] for the critical exponents, namely, $\beta = 0.3265(3)$, $\nu = 0.63002(10)$, and $\gamma = 1.2372(5)$. The quality of the achieved data collapse was also used to improve the accuracy of the previously determined critical temperature by means of a carefully viewed inspection, estimating a value of $T_c = 6.208(4)$ since tiny and systematic deviations are observed for different temperatures (not shown here for the sake of space). It is worth mentioning that we are not aware of other estimations of T_c for this lattice. On the other hand, the obtained collapses are quite satisfactory and strongly support not only the critical exponents chosen but also the fact that we must keep the aspect ratio constant, as already discussed along Sec. III. In fact, attempts to collapse data taken for different values of C were unsuccessful (not shown here for the sake of space).

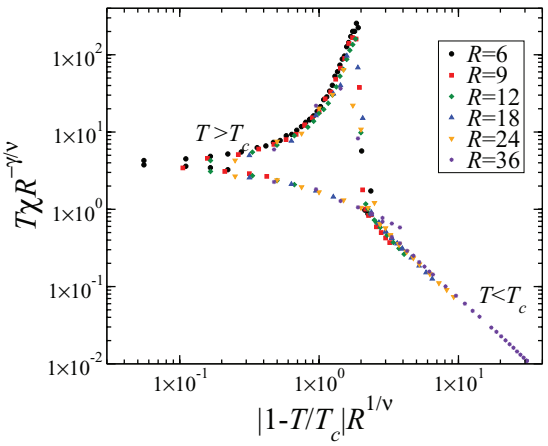

FIG. 7. Scaling plot of the susceptibility as obtained in a log − log plot, according to Eq. (9) by using the data already shown in Figure 2 and taking $T_c = 6.208$, $\nu = 0.63002$, and $\gamma = 1.2372$.

Furthermore, the scaling statements can be further supported by a more interesting test, i.e., the scaling ansatz given by Eq. (14), namely, the verification of the dependence of $\langle M \rangle R^{\beta/\nu}$ on the square root of the aspect ratio C at criticality (cf. Figure 8), since under this condition the first scaling argument of Eq. (8) simply vanishes, i.e., $\epsilon R^{1/\nu} \equiv 0$. As can be observed in Figure 8, data obtained for cylinders of different sizes but sharing the same aspect ratio have almost the same vertical axis, i.e., $\langle M \rangle L^{\beta/\nu}$ is practically constant, in full agreement with the data collapse already obtained in Figure 5. The best fit of the data yields a slope of 0.486(6), where the error bar merely reflects the statistical error. So, we conclude that the agreement with the predicted scaling behaviour is excellent, provided that the errors in the determination of T_c, as well as corrections to scaling, are not considered.

Let us now analyse the data corresponding to measurements of the spin-spin correlation function as obtained at criticality. Figure 9(a) shows log-linear plots of $g(l)$ *versus* l as obtained for cylinders of different radii, R. The exponential decay of $g(l)$ is verified by fitting the curves according to Eq. (18). In this way, we determine the characteristic lengths, $\xi(R)$, which are plotted as a function of R in the inset of Figure 9(a). Also, Figure 9(b) shows that the data already displayed in Figure 9(a) can be collapsed according to Eq. (20), where we used $\eta = 0.03627$ for the exponent of the correlations decay.[43]

As already discussed in Sec. III, the exponential decay of $g(l)$ is due to the formation of a multi-domain structure that takes place close to criticality. In order to observe the expected alternating multi-domain pattern in snapshot configurations, a coarse-graining procedure must be done. For this purpose, each point of the coarse-grained (CG) snapshots shown in Figure 10 represents the average magnetization of a 4-site-long slit (taken along the axis of the pore). This averaging method not only shortens the length of the pore, from

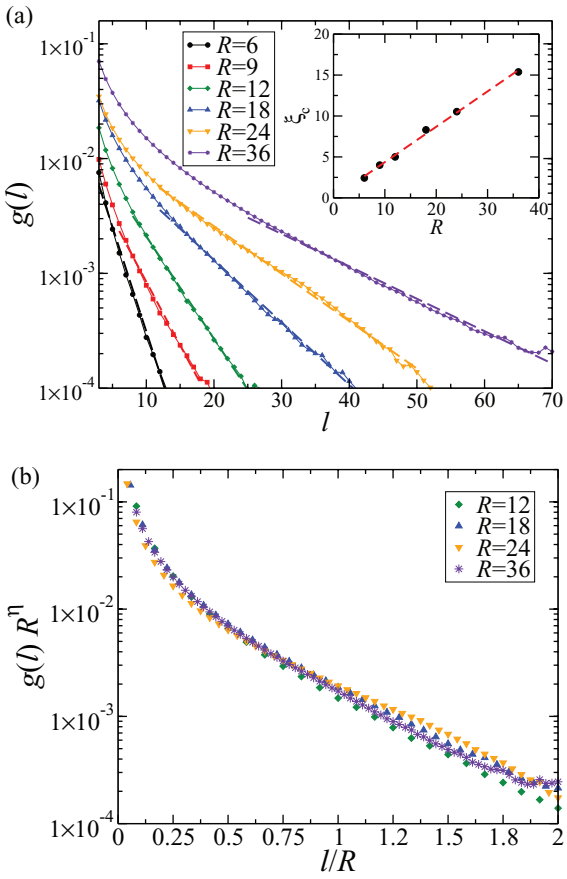

FIG. 9. (a) Log-linear plot of the axial correlation function, $g(l) = \frac{1}{N_l}\sum_{k=1}^{L/2} s(k)s(k+l)$ *versus* l, the distance between spins, as obtained at the critical temperature. The aspect ratio $C \equiv R/L$ is kept constant in all cases. By fitting the correlation function according to Eq. (18) (see the dashed lines in the main panel) we obtain the characteristic correlation lengths, $\xi(R)$, which are shown in the inset as a function of the radius of the pores. The slope of the linear function relation between the characteristic length and the radius shown by the full line is 0.43(2). (b) Scaling plot of the data already shown in (a) as obtained according to Eq. (20). More details are given in the text.

$L = 216$ to $L_{CG} = 54$ in the case of the pore shown in Figure 10, but also projects the pore onto a plane. In fact, averages over lines of the triangular lattice planes that are perpendicular to the axis of the pore are also taken. In the snapshot configurations of Figure 10, at low temperatures the magnetization along the cylinder is rather uniform (cf. Figure 10(a)) and only two main domains are present, as expected for the ordered phase. However, by approaching the size-dependent effective critical temperature, one observes the formation of alternating domains of different magnetization (cf. Figure 10(b)), while at $T_C(R = 18) \simeq 6.1$ the system clearly exhibits a multi-domain pattern (cf. Figure 10(c)). So, within the multi-domain regime, far from the ordered phase, the inter-domain distance is just given by $\xi(R)$ (cf. Figure 9).

Coming back to the behaviour of the characteristic lengths of the alternating domains (cf. the inset of Figure 9), the best fit of our results yields $\xi(R) \propto R$ with a proportionality constant $B = 0.43(2)$. It is worth mentioning that the value of the proportionality constant cannot be fixed by any simple phenomenological scaling argument and it depends on the boundary conditions used. In the case of 2D strips B can

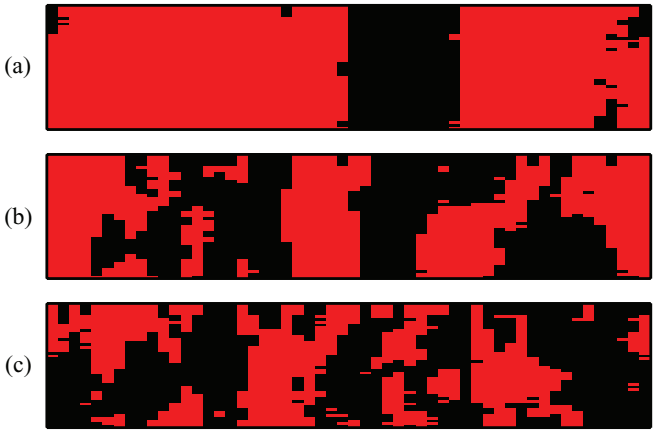

FIG. 10. Typical (coarse-grained) snapshot of a tube of radius $R = 18$ taken at different temperatures: (a) $T = 6.08$, (b) $T = 6.1$, and (c) $T = 6.28$. Notice that at temperatures close to the effective critical temperature $T_C(R = 18) \simeq 6.1$, the system exhibits a multi-domain pattern, which is lost for temperatures far below (above) $T_C(R = 18)$. Details of the coarse-graining procedure are given in the text.

be calculated exactly by means of conformal invariance[5,40] as well as estimated by Monte Carlo simulations.[44] In fact for 2D strips with free boundary conditions one has $B = 2/\pi \simeq 0.63$.[40] Our value of B for 3D tubes with free boundary conditions is slightly lower than in the 2D case, and we are not aware of any previous estimation of the constant in the 3D case for the lattice used in this paper. However, for the simple cubic lattice of dimension L with periodic boundary conditions it has been found[43] that $\xi/L = 0.6431(1)$. It is also worth noticing that the estimated value of B may still have a residual dependence on the finite aspect ratio used in this work.

Figures 11(a) and 11(b) show plots of the radial magnetization profiles *versus* the distance to the centre of the cylinders, as obtained for different temperatures and for $R = 6$ and $R = 36$, respectively. For the case of the smaller cylinder, and for the low temperature regime, $T < T_C(R = 6) \approx 5.58$, one observes that the magnetization decreases monotonically and rather sharply when one goes from the bulk towards the surface of the pore. On the other hand, for higher temperatures, e.g., $T > 5.6$ in Figure 11(b), the magnetization decreases rather smoothly. On the other hand, for the larger tube ($R = 36$) the magnetization remains constant by adopting the value of the bulk even far from the centre of the cylinder, e.g., up to $r = 20$ for $T = 6.0$, but the distance increases when the temperature decreases (cf. Figure 9(b)). Here, and particularly for the low-temperature regime, the drop in the magnetization spreads over few lattice spaces only, so that the effective critical temperature is slightly shifted downwards, as evidenced by the behaviour of the whole magnetization (cf. Figure 1).

The dramatic suppression of the order close to the boundaries of the system is an expected feature of critical behaviour at surfaces.[46,47] In fact, it is known that the surface of the system undergoes an ordinary phase transition, when the temperature is decreased but the surface order is not observed, even for $T < T_c$. This phase transition arises due to the missing neighbours of sites laying on the surface. In other words, the fact that spins placed at the surface of the tube have less nearest-neighbours, as compared to 8 in the bulk, strongly suppresses the surface ordering. Furthermore, due to that

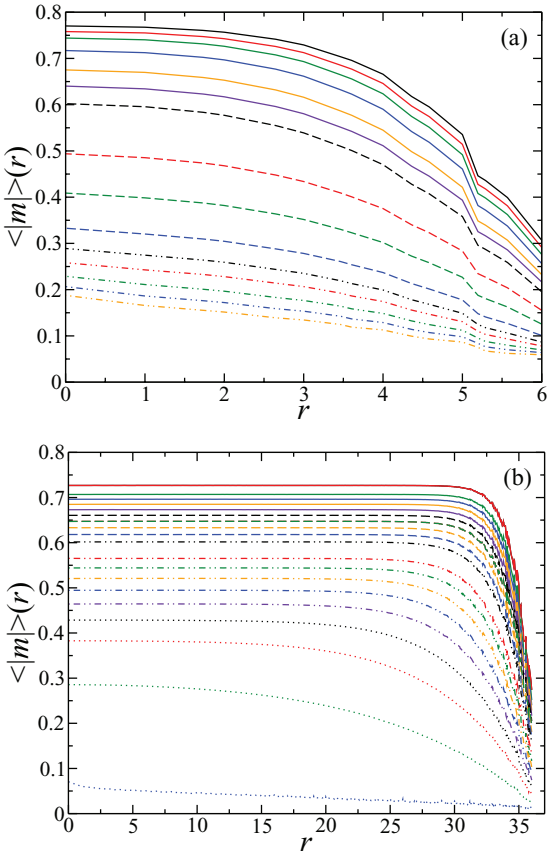

FIG. 11. Plots of magnetization profiles measured for pores of different radii: (a) $R = 6$ and $5.32 \leq T \leq 5.88$; (b) $R = 36$ and $5.36 \leq T \leq 6.16$. In both cases the aspect ratio $C \equiv R/L = 1/12$ is kept constant and the temperature increases from top to bottom with steps of $\Delta T = 0.04$. For more details see text.

effect, one observes not only a large drop in the effective critical temperature, but also an overall shift of the whole magnetization of the tube towards lower temperatures, as already shown in Figure 1.

A characteristic quantity of surface phenomena is the extrapolation length, λ, which appears as a constant in the surface term of the Landau semi-infinite ferromagnet free energy.[46] In particular, this model predicts that close to the surface the order parameter varies linearly with the distance to the boundary, as it can be already observed in the magnetization profiles of Figures 11(a) and 11(b). By performing a linear extrapolation of the order parameter beyond the surface, the distance where it vanishes can be determined and the so-called extrapolation length can be defined.[47]

As discussed in Refs. 46 and 47, only within a mean field scheme where fluctuations might be neglected, it makes sense to consider that λ is temperature independent. If the system is close to criticality this scheme fails and a size-scale and temperature dependent extrapolation length must be considered. This behaviour is observed in Figure 12 where, for pores of different sizes, λ is plotted against temperature. As long as the temperature is lower than the effective critical temperature, the extrapolation length is flat, in agreement with the mean-field predictions. However, as T gets closer and exceeds the effective critical temperature, λ increases. In addition, the increment of λ is bigger for bigger pores, as it is clearly observed for the three bigger tubes. The value of λ in the flat

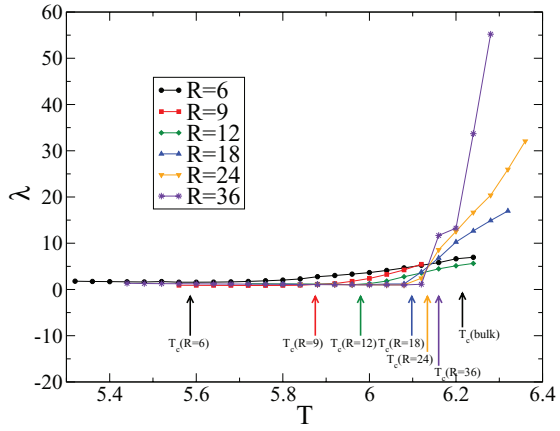

FIG. 12. Plot of the extrapolation length (λ) vs. temperature (T), as obtained for pores of radii $R = 6$, 9, 12, 18, 24, and 36. For each pore size, the extrapolation length is flat for temperatures lower than the effective critical temperature, where each one is indicated with an arrow, but increases when T is bigger than the latter. This behaviour shows that as far as fluctuations are negligible the extrapolation length is independent of temperature. For more details see text.

region is, for all pores, close to the lattice spacing, a, as expected for d-dimensional Ising models away from the critical region.[48]

In order to give a qualitative insight into the suppression of surface ordering, in Figure 13 we present 3D snapshots of

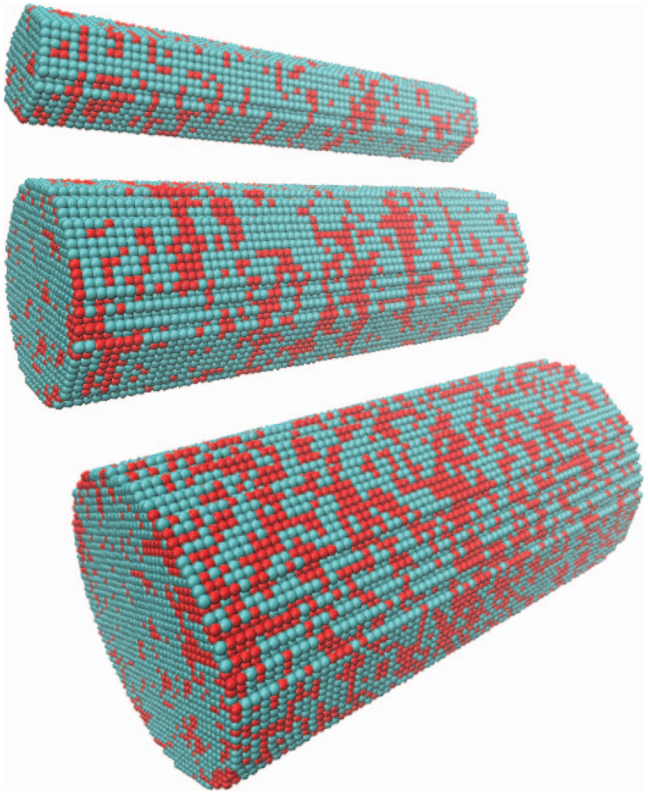

FIG. 13. 3D snapshots of a tube of radius $R = 18$ and aspect ratio $R/L = 1/12$ obtained at $T = 6.06 < T_c(R = 18) = 6.10$. The top and medium panels show the inner cores of the tube obtained by removing outer layers with $r > 6$ and $r > 12$, respectively. Also, the lowest panel shows the surface of the tube with $R = 18$. In this way, one observes that the surface does not exhibit a clear order as in the case of the inner layer ($r = 6$). This behaviour is consistent with the magnetization profiles shown in Figure 9 where a dramatic drop in magnetization close to the surface is observed. For more details see text.

the system rendered using VMD software,[45] where occupied (spin up) and empty (spin down) sites are depicted with different colours. In order to enhance the view, a coarse-grain procedure must also be performed. Accordingly, each point of the coarse-grained snapshot represents the average magnetization of a 4-site-long slit taken along the axis of the pore. This averaging method shortens the length of the pore from 216 to 54 as shown in Figure 13. By removing the outer layers of the tube, one can observe that a disordered surface with $R = 18$ (Figure 13, low panel) changes to ordered ones, e.g., for inner layers $r = 12$ and $r = 6$, as shown in the middle and upper panels of Figure 13, respectively.

V. CONCLUSIONS

We performed numerical Monte Carlo simulations of the Ising ferromagnet confined in quasi-cylindrical pores of radius R and length L. The obtained results can be rationalized in terms of the standard finite-size scaling theory where, in comparison to the most simple scaling laws, two modifications have to be introduced: (a) Now the scaling functions depend on the isotropic correlation length ξ, as well as on L and R. In this way, by using well-established properties of homogeneous functions one finds that it is necessary to deal with an additional scaling argument, namely, the aspect ratio $C \equiv R/L$, which in turn needs to be kept constant in order to achieve proper data collapse of the numerical data. (b) For $L \to \infty$, $R \to \infty$, but keeping $R/L = constant$, and $T < T_c$ the axial correlation function has a simple exponential decay.

In our simulations, the geometry of the pores is achieved by replicating L-times triangular lattice discs of radius R. So, our extrapolations to the thermodynamic limit of the size-dependent effective critical temperatures yields $T_c(\infty) = 6.208(4)$, i.e., a value above the critical temperature of the 3D Ising model on the square lattice ($T_{c_{SL}}(\infty) = 4.51142(5)$) and higher than the critical point reported for the pure 2D triangular lattice, namely, $T_{triang_{2D}} \approx 3.641$ but close to the reported value of the critical temperature for the 4D hyper-cubic lattice $T_{hypercub_{4D}} \approx 6.682$.

By measuring magnetization profiles along the inner radii of the tubes, one observes the strong suppression of surface ordering caused by the free boundary of the sample, leading to the observation of an ordinary surface transition. Extrapolations of the magnetization profiles away from the surface allow us to determine the so-called "extrapolation length," which is found to behave according to a mean-field theory at low enough temperature where fluctuations are irrelevant. Furthermore, this surface effect causes the rounding of the total magnetization of the pores, which is additionally largely shifted towards lower temperatures when the radii of the samples decrease due to finite-size effects. These effects are also evidenced by dramatic shifts in the peaks of the susceptibility and the specific heat. However, by properly keeping the aspect ratio of the sample $C \equiv R/L$ constant, we achieved satisfactory data collapse of relevant observables, as expected from finite-size scaling arguments.

On the other hand, measurements of the axial correlation length are consistent with the formation of alternating domains of opposite magnetization along the axis of the tubes. This statement is further supported by drawing proper snapshot configurations. It is found that the typical average size of these domains depends linearly on R (keeping the aspect ratio $C \equiv R/L =$ constant), more specifically we found $\xi = 0.43R$.

ACKNOWLEDGMENTS

We acknowledge financial support from CONICET, UNLP, and CIC de la Provincia de Buenos Aires (Argentina).

[1] J. K. Singh and S. K. Kwak, J. Chem. Phys. **126**(2), 024702 (2007).
[2] D. Takaiwa, I. Hatano, K. Koga, and H. Tanaka, Proc. Natl. Acad. Sci. U.S.A. **105**, 39 (2008).
[3] I. Brovchenko, A. Geiger, and A. Oleinikova, J. Chem. Phys. **120**(4), 1958 (2004).
[4] C. Chen, M. Ma, K. Jin, J. Z. Liu, L. Shen, Q. Zheng, and Z. Xu, Phys. Rev. E **84**, 046314 (2011).
[5] J. L. Cardy, *Scaling and Renormalization in Statistical Physics* (Cambridge University Press, Cambridge, 1996).
[6] V. Privman, *Finite Size Scaling and Numerical Simulation of Statistical Systems* (World Scientific, Singapore, 1990).
[7] G. J. Zarragoicoechea and V. A. Kuz, Phys. Rev. E **65**, 021110 (2002).
[8] M. N. Barber, *Phase Transitions and Critical Phenomena* (Academic Press, New York, 1983).
[9] C. Alba-Simionesco, B. Coasne, G. Dosseh, G. Dudziak, K. E. Gubbins, R. Radhakrishnan, and M. Sliwinska-Bartkowiak, J. Phys. C.: Condens. Matter **18**, R15 (2006).
[10] A. Winkler, D. Wilms, P. Virnau, and K. Binder, J. Chem. Phys. **133**, 164702 (2010).
[11] L. Boinovich and A. Emelyanenko, Mol. Phys. **107**, 1745 (2009).
[12] A. O. Parry and R. Evans, Phys. Rev. Lett. **64**, 439 (1990).
[13] A. C. Dillon and M. J. Heben, Appl. Phys. A **72**, 133 (2001).
[14] L. Xinlei, Europhys. Lett. **100**, 46002 (2012).
[15] Y. Xu, K. Jang, T. Yamashita, Y. Tanaka, K. Mawatari, and T. Kitamori, Anal. Bioanal. Chem. **402**, 99 (2012).
[16] R. Saito, G. Dresselhaus, and M. S. Dresselhaus, *Physical Properties of Carbon Nanotubes* (Imperial College Press, 1999).
[17] M. E. Fisher and R. J. Burford, Phys. Rev. **156**, 583 (1967).
[18] A. Milchev, A. De Virgilis, and K. Binder, J. Phys. C.: Condens. Matter **17**, 6783 (2005).
[19] M. R. Swift, A. L. Owczarek, and J. O. Indekeu, Europhys. Lett. **14**, 475 (1991).
[20] E. V. Albano and K. Binder, Phys. Rev. Lett. **109**, 036101 (2012).
[21] M. N. Popescu, G. Oshanin, S. Dietrich, and A.-M. Cazabat, J. Phys. C.: Condens. Matter **24**, 243102 (2012).
[22] E. V. Albano, K. Binder, D. Heermann, and W. Paul, Surf. Sci. **223**, 151 (1989).
[23] A. De Virgilis, R. L. C. Vink, J. Horbach, and K. Binder, Europhys. Lett. **77**, 60002 (2007).
[24] A. Milchev, M. Müller, K. Binder, and D. P. Landau, Phys. Rev. E **68**, 031601 (2003).
[25] D. B. Abraham and A. Maciołek, Phys. Rev. Lett. **89**, 286101 (2002).
[26] E. V. Albano, K. Binder, and W. Paul, J. Phys. C.: Condens. Matter **12**, 2701 (2000).
[27] D. Wilms, A. Winkler, P. Virnau, and K. Binder, Phys. Rev. Lett. **105**, 045701 (2010).
[28] E. V. Albano, K. Binder, D. W. Heermann, and W. Paul, Z. Phys. B: Condens. Matter **77**, 445 (1989).
[29] M. E. Fisher, Rev. Mod. Phys. **46**, 597 (1974).
[30] M. E. Fisher and P. G. de Gennes, C. R. Acad. Sci. Paris Ser. B **287**, 207 (1978).
[31] M. Krech, J. Phys.: Condens. Matter **11**, R391 (1999).
[32] A. Gambassi, J. Phys.: Conf. Ser. **161**, 012037 (2009).
[33] M. Henkel, H. Hinrichsen, and S. Lübeck, *Non-equilibrium Phase Transitions: Absorbing Phase Transitions Theoretical and Mathematical Physics* (Springer, London, 2008).
[34] K. Binder, Rep. Prog. Phys. **60**, 487 (1997).
[35] K. Binder, *Computational Methods in Field Theory: Proceedings of the 31. Internationale Universitätswochen für Kern- und Teilchenphysik, Schladming, 1992*, edited by H. Gausterer and C. B. Lang (Springer, Berlin Heidelberg, 1992), Vol. 409, p. 59.

[36]K. K. Mon and K. Binder, J. Chem. Phys. **96**, 6989 (1992).
[37]A. M. Ferrenberg and D. P. Landau, Phys. Rev. B **44**, 5081 (1991).
[38]M. E. Fisher, Phys. Soc. Jpn. Suppl. **26**, 87 (1969).
[39]M. E. Fisher and V. Privman, J. Stat. Phys. **33**, 385 (1983).
[40]J. L. Cardy, J. Phys. A: Math. Gen. **17**, L385 (1984).
[41]M. E. Fisher, Rep. Prog. Phys. **30**, 615 (1967).
[42]D. S. Gaunt, M. F. Sykes, and S. McKenzie, J. Phys. A **12**, 871–877 (1979).
[43]M. Hasenbusch, Phys. Rev. B **82**, 174433 (2010).
[44]M. Hasenbusch, Phys. Rev. B **83**, 134425 (2011).
[45]W. Humphrey, A. Dalke, and K. Schulten, J. Mol. Graphics **14**, 33 (1996).
[46]K. Binder, *Phase Transitions and Critical Phenomena*, edited by C. Domb and J. L. Lebowitz (Academic, London, 1983), Vol. 8, p. 1.
[47]H. W. Diehl, *Phase Transitions and Critical Phenomena*, edited by C. Domb and J. L. Lebowitz (Academic, London, 1986), Vol. 10, p. 75.
[48]M. E. Fisher, J. Vac. Sci. Technol. **10**, 665 (1973).